

AD-A250 853

Publ
gath
coll
Down



ION PAGE

Form Approved
OMB No. 0704-0188

2

age 1 hour per response, including the time for reviewing instructions, searching existing data sources, the collection of information. Send comments regarding this burden estimate or any other aspect of the Washington Headquarters Services, Directorate for Information Operations and Reports, 1215 Jefferson Management and Budget, Paperwork Reduction Project (0704-0188), Washington, DC 20503.

1. AGENCY USE ONLY (Leave Blank)

20 April 1992

3. REPORT TYPE AND DATES COVERED
Final 15 Mar '89 to 14 Mar '92

4. TITLE AND SUBTITLE

Laser Material Interaction

5. FUNDING NUMBERS

Grant No.
AFOSR-89-0337

6. AUTHOR(S)

S.R.J. Brueck

DTIC
EFFECTIVE
S C
MAY 19 1992
D

7. PERFORMING ORGANIZATION NAME(S) AND ADDRESS(ES)

The University of New Mexico
Center for High Technology Materials
EECE Building, Room 125
Albuquerque, NM 87131-6081

8. PERFORMING ORGANIZATION
REPORT NUMBER

AFOSR- 02 0367

9. SPONSORING/MONITORING AGENCY NAME(S) AND ADDRESS(ES)

Department of the Air Force
Air Force Office of Scientific Research
Building 410
Bolling AFB, DC 20332-6448

10. SPONSORING/MONITORING
AGENCY REPORT NUMBER

2301/AS

11. SUPPLEMENTARY NOTES

12a. DISTRIBUTION/AVAILABILITY STATEMENT

92-12951



Unlimited

13. ABSTRACT (Maximum 200 words)

The Laser-Materials Interaction Laboratory at the Center for High Technology Materials of the University of New Mexico is devoted to the study of a broad range of laser spectroscopic probes of semiconductor and nonlinear materials, fabrication processes and optoelectronic devices. Much of this work is being carried out in conjunction with the Optoelectronics Research Center Program at CHTM, which is also partially funded by the Air Force Office of Scientific Research. Significant progress has been made during this reporting period in a number of areas including: ultrafast operation of optically-pumped resonant periodic-gain GaAs surface-emitting lasers; grating coupling to surface-plasma waves; nonlinear optics of PLZT films and SiO_2 , and confocal microscopy for the direct measurement of semiconductor transport parameters.

14. SUBJECT TERMS

Optoelectronic devices, laser spectroscopic probes of semiconductor and nonlinear materials

15. NUMBER OF PAGES

16. PRICE CODE

17. SECURITY CLASSIFICATION
OF REPORT

18. SECURITY CLASSIFICATION
OF THIS PAGE

19. SECURITY CLASSIFICATION
OF ABSTRACT

20. LIMITATION OF ABSTRACT
UL

NSN 7540-01-280-5500

55 1 2 078

Standard Form 298 (Rev 2-89)
Prescribed by ANSI Std Z39-18
200 107

Final Technical Report
Laser-Material Interactions
for the period
March 15, 1991 to March 14, 1992
Grant No. AFOSR 89-0337

Principal Investigator

Professor S. R. J. Brueck
Center for High Technology Materials
University of New Mexico
Albuquerque, NM 87131

Accession No.	Ref. No.
Serial No.	Date
Dist. Code	Page
Classification	
By	
Distribution	
Availability Codes	
Dist	Level and/or Special
A-1	



CHARACTERIZATION OF THIN Al FILMS USING GRATING COUPLING TO SURFACE PLASMA WAVES

Saleem H. Zaidi, D. W. Reicher, B. Draper¹, J. R. McNeil,² and S. R. J. Brueck³

Center for High Technology Materials, University of New Mexico

Albuquerque, NM 87131

ABSTRACT

A detailed characterization of the optical, microstructural and electrical properties of thin (5-50 nm) Al films grown by thermal evaporation, magnetron sputtering, and ion-assisted sputtering (IAS), is reported. Dielectric-function measurements were carried out by using grating coupling to surface plasma waves (SPW) and, for comparison, ellipsometric measurements were also performed. Scanning electron microscope (SEM) studies of film microstructure as well as dc electrical resistivity measurements were carried out and correlated with the optical data. Using the Bruggeman effective media approximation, good agreement was obtained for thicker films (30-50 nm), but not for thinner films (< 30 nm). SEM and resistivity measurements suggest that conditions of film growth influence the behavior of individual grains, resulting in increased electron reflectance at the grain boundaries with increasing energy delivered to the substrate during deposition. This resulted in lower electrical resistivities for evaporated films than for IAS films. Finally, the influence of 5-20 Å Al₂O₃ on thick Al films was investigated, both SPW and resistivity measurements suggest that the oxide film was not confined to film surface, but had penetrated inside the film leading to much higher electrical resistivities than would be otherwise expected.

*To be published
submitted to Jour. of Appl. Phys. Mar 1981*

1. INTRODUCTION

Optical characterization of metal films is important for process control in the semiconductor industry. The standard ellipsometric and reflectometric techniques [1-4] possess the requisite sensitivity but require complex instrumentation and computations, in addition, a very careful and model dependent interpretation of the data is necessary for determining the optical parameters. A waveguide approach, using prism coupling to either dielectric waveguide modes [5] or to a surface-plasma-wave confined to a metal-dielectric interface [6-8] has also been used. The optical excitation of surface plasma waves (SPWs) has been carried out in both Kretschmann-Raether geometry [9] or in Otto geometry [10]. In the Kretschmann-Raether geometry, SPW excitation occurs by tunneling thru a thin metal film, which places severe constraints on the film thickness and dielectric constants, limiting its effectiveness mostly to Ag and Au films, and, of course, on the transparent substrate material which is typically a glass prism. In the Otto geometry the prism is placed in close proximity of the top surface of the film. The tunnel barrier between the metal film and the prism has to be very thin (< 500 nm) requiring significant pressure between the prism and the substrate. Both of these techniques are sensitive to film properties, and the theoretical formalism is provided by Fresnel theory.

Grating-coupling based characterization, in contrast, is free of all the above mentioned constraints. The theoretical formalism to describe the coupling process is, however, complex and requires detailed computational algorithms[11-12]. Recently, we have presented a detailed analysis of grating coupling to SPWs for a wide range of grating depths and profiles [13-14]. The theoretical analysis, based on the Rayleigh expansion, was very simple and provided good agreement with the experimental data. Here, we apply this analysis to measurement of metal film optical properties. Al films because of their importance in integrated circuit technology were used. These films were deposited by three different deposition techniques; thermal evaporation, magnetron sputtering, and ion-assisted magnetron sputtering. In addition, ellipsometric, resistivity, and SEM measurements were also carried out on these films to compare with the SPW data. In all cases, excellent agreement with SPW measurements was obtained.

2. EXPERIMENTAL ARRANGEMENT

An Al target was used which was 99.99 % pure. Room temperature depositions were carried out in a 45-cm diameter, cryogenically pumped bell jar vacuum system [15]. For thermal evaporation, a tungsten boat was used. Sputtered films were deposited at 0.5 mTorr Ar pressure using a planar magnetron source. For ion-assisted deposition, a beam of argon ions from a Kaufman ion source was directed at the substrate surface during magnetron sputtering. The beam voltage was maintained at 440 eV, and ion flux at the film surface was approximately $25 \mu\text{Amp}/\text{cm}^2$. In all cases, depositions were carried out at a rate $\sim 2 \text{ \AA/s}$, starting vacuum was in the low 10^{-7} Torr range, and the film thickness was determined by a crystal monitor. The ellipsometric measurements were performed on films deposited on Si-wafers. For SPW measurements, the films were deposited on holographically defined submicrometer gratings on Si [16]. The zero order reflectance ($\lambda=633 \text{ nm}$) from the coated gratings was monitored as a function of incident angle, the excitation of surface plasma waves is manifested by resonance like dip in the reflectance curve, and is described in detail elsewhere [13-14].

3. ELLIPSOMETRIC MEASUREMENTS

Ellipsometry involves measurement of the effect of reflection on the state of polarization of the reflected light [1]. The state of polarization is characterized by the phase and the amplitude relationships between the two orthogonal polarizations of the electric field vector of the polarized field. The electric field orientation of one, designated as TM, is in the plane of incidence, and of the other, designated as TE, is normal to the plane of incidence. In general, reflection causes a change in the relative phases of the TM and TE waves, and a change in the ratio of their amplitudes. The angle Δ is defined as the change in phase, and the angle Ψ as the arctangent of the factor by which the amplitude ratio changes. The angles Δ and Ψ are measured by the ellipsometer. There are a wide variety of commercial software packages which calculate the film dielectric constants and thickness, given Δ , Ψ , the light wavelength, and the substrate index. From our measurements, the dielectric constants were calculated by using a computational package developed by Urban [17]. Fig. 1 shows the measured variation of Ψ

and Δ as a function of film thickness, the values at zero thickness correspond to those of Si. The qualitative behavior of ψ is the same for the films deposited by all three techniques. The behavior of Δ , however, is similar for sputtered and ion-assisted sputtered (IAS) films, but for evaporated films it remains approximately constant. Using these Δ and ψ values, the dielectric constants of Table 1 were calculated. The real part of the dielectric constant shows much larger changes than the imaginary part. Also, the real and imaginary dielectric constants for evaporated and sputtered films were larger than for IAS films.

4. SPW MEASUREMENTS

In Figs. 2 and 3, we show a sequence of 0-order reflectance scans of sputtered Al films as thickness is increased approximately from 5 to 50 nm on Si grating ($d=477$ nm, depth=16 nm). The dotted curves present the results of the best fit to experimental lineshape, and will be discussed below. The main features of Fig. 2, where the film thickness varies from about 5 to 20 nm can be characterized as follows:

1. the appearance of a broad SPW resonance at film thickness of 11 nm with intensity minimum at $\theta = 18.08^\circ$ and a cusp at $\theta = 18.9^\circ$ due to the emergence of the -1-diffraction order (i.e., for angles greater than 18.9° there is an allowed -1-diffraction order that can take energy from the reflected beam, for angles less than 18.9° this order is evanescent);
2. the decrease in SPW resonance width from about 1.5° (Fig. 2b) to $.9^\circ$ (Fig. 2 d);
3. the increase in coupling efficiency from 0.1 (Fig. 2b) to 0.3 (Fig. 2d) and;
4. the slight shift in resonance angles (angles at which intensity minima occur) to larger angular values, i.e., a decrease in angular separation between SPW resonance angle and the cusp angle (the cusp angle remains constant determined by only by grating periodicity and the laser wavelength).

The behavior of the SPW resonance for thicker films (24-50 nm) is shown in Figure 3, and can be briefly summarized as follows:

1. the continuing decrease in SPW resonance width from 0.86° (Fig. 3a) to 0.57° (Fig. 3d);
2. the saturation of coupling efficiency at 0.52 (Figs. 3 c&d) from 0.34 (Fig. 3a) and;
3. the continuing small shifts in resonance angles to larger angular values.

In Fig. 4, we have plotted coupling efficiency, resonance width, and the resonance angle shifts as a function of film thickness for films deposited using all three deposition techniques. The salient features of these measurements are :

1. the coupling efficiencies reach ~ 52 % for both evaporated and sputtered films for film thickness in the range 30-40 nm, while for the IAS films, the corresponding efficiency was ~ 41 % for film thickness of above 50 nm ;
2. the resonance widths for the evaporated and sputtered films are almost identical, while those for IAS films were approximately 15 % larger and;
3. the absolute shifts in the resonance angles (i.e., the angular difference between SPW resonance and the cusp angle) decreased from 0.78° to 0.74° for evaporated films, and from 0.82° to 0.76° for sputtered films, while for IAS films weak dependence with film thickness was observed.

In general, the evaporated and sputtered films were observed to have similar characteristics, while the IAS films showed significantly different patterns. In contrast with the ellipsometric measurements where there were two observable quantities, the SPW measurements provide three observed quantities, the resonance width, resonance angle, and the coupling efficiency. In addition the variations in optical properties for the different films are more evident in these measurements than they were in the ellipsometric measurements

5. THEORETICAL MODELING

The grating coupling to SPWs has been treated by a large number of authors [11-13]. Most of these theoretical formalisms are very complex, and require extensive computational efforts. Here, we have used an elegant and simple analysis for SPWs at a single grating interface with any arbitrary profile developed by Toigo et al. [18]. We have extended this analysis to two interfaces to model optically thin films. The theoretical analysis is based on the Rayleigh hypothesis and is briefly reviewed here.

For TM-polarized light incident at a grating surface at an angle θ , we can write the magnetic field in the three regions (vacuum, metal film, and Si-substrate) as follows:

$$B_{vac}(y, z) = \exp(i(k_y y + k_z z)) + \sum_n R_n \exp(i(k_n y - \alpha_n z)); \quad 1.$$

$$B_{met}(y, z) = \sum_n [A_n \exp(i(k_n y + \beta_n z)) + B_n \exp(i(k_n y - \beta_n z))]; \quad 2.$$

$$B_{sub}(y, z) = \sum_n C_n \exp(i(k_n y + \gamma_n z)); \quad 3.$$

where

$$\begin{aligned} k_y &= k \sin \theta, & k_z &= k \cos \theta, & k &= \omega / c; \\ k_n &= k_y + n g, & n &= 0, \pm 1, \pm 2, \dots, & g &= 2 \pi / d; \\ \alpha_n^2 &= k^2 - k_n^2, & \beta_n^2 &= \epsilon_{met} k^2 - k_n^2, & \gamma_n^2 &= \epsilon_{sub} k^2 - k_n^2. \end{aligned} \quad 4.$$

and ϵ_{met} , ϵ_{sub} are metal and substrate (Si) dielectric constants, and d is the grating period. For a grating profile defined by $f(y)$, a straightforward application of electromagnetic boundary conditions leads to the following set of coupled linear differential equations (as explained in the appendix):

$$\sum_n [-R_n X_{m-n}(-\alpha_n u) + A_n X_{m-n}(\beta_n u) + B_n X_{m-n}(-\beta_n u)] = X_m(k_z u); \quad 5.$$

$$\sum_n [A_n X_{m-n}(\beta_n u) \exp(i \beta_n t) + B_n X_{m-n}(-\beta_n u) \exp(-i \beta_n t) - C_n X_{m-n}(\gamma_n u)] = 0; \quad 6.$$

$$\begin{aligned} \sum_n [R_n \left(\frac{(\omega/c)^2 - k_m k_n}{\alpha_n} \right) X_{m-n}(-\alpha_n u) + A_n \left(\frac{\epsilon_{met}(\omega/c)^2 - k_m k_n}{\epsilon_{met} \beta_n} \right) X_{m-n}(\beta_n u) \\ + B_n \left(\frac{\epsilon_{met}(\omega/c)^2 - k_m k_n}{\epsilon_{met} \beta_n} \right) X_{m-n}(-\beta_n u)] = \left(\frac{(\omega/c)^2 - k_m k_y}{k_z} \right) X_m(k_z u); \end{aligned} \quad 7.$$

$$\begin{aligned} \sum_n [A_n \left(\frac{\epsilon_{met}(\omega/c)^2 - k_m k_n}{\epsilon_{met} \beta_n} \right) X_{m-n}(\beta_n u) \exp(i \beta_n t) + B_n \left(\frac{\epsilon_{met}(\omega/c)^2 - k_m k_n}{\epsilon_{met} \beta_n} \right) X_{m-n}(-\beta_n u) \exp(-i \beta_n t) \\ - C_n \left(\frac{\epsilon_{sub}(\omega/c)^2 - k_m k_n}{\epsilon_{sub} \gamma_n} \right) X_{m-n}(\gamma_n u)] = 0; \end{aligned} \quad 8.$$

where $X_p(p)$ is the Fourier transform of the grating profile defined by

$$X_p(p) = \frac{1}{d} \int_{-d/2}^{d/2} \exp(-i pgy) \exp(i p f(y)) dy. \quad 9.$$

Here p ($=m-n$) is an integer and p is given by $\alpha_n u$, $\beta_n u$, or $\gamma_n u$. In Eqs. 5-8 both n and m go from $-\infty$ to $+\infty$.

Computationally, however, the series is truncated at values for which inclusion of next higher order term does not result in any change of the previously calculated value. The Fourier transform integral can be evaluated for any given grating profile. In particular, for sinusoidal profiles eq. 9 gives the familiar Bessel function expansion, and has been investigated in detail elsewhere [13]. Convergence for this particular profile is obtained for $n,m = 2$. For other nonanalytical profiles, i.e., square or rectangular, the Rayleigh assumption is usually not valid, however, it was pointed out by Hill et al. [19] that for shallow gratings ($u/d = .07$), this method can still be applied with reliable results. In our numerical calculations, we have tested for consistent results for n,m as large as 10 leading to an 84×84 matrix inversion. For numerical calculations, the grating profile used for evaluating the integral Eq. 9 is shown in Fig. 5 (see appendix for more details). The actual SEM profile of Si grating (depth = 16 nm) used in the experiments is shown in Fig. 8c. The real and imaginary parts of the dielectric constant of Al were allowed to vary independently to obtain the best fit to the experimentally observed resonance lineshapes. The shift in the resonance angle was strongly dependent on the real part of the dielectric constant, the width of the resonance was a function of both the real and imaginary parts of the dielectric constant. Also a 5% variation in either the film thickness or the grating depth did not result in a shift of the resonance angle.

6. COMPARISON OF ELLIPSOMETRIC AND SPW DATA

In Table 1, we have compared the dielectric constants calculated by the two different techniques. For film thickness below 10 nm, the metal films did not show the characteristic SPW lineshape, therefore it was not possible to calculate the corresponding dielectric constants. The comparison of the data shows that, in general, the values calculated from the two methods were within 6% of each other, although for some cases, especially for ~

10-nm thick films, the difference was much larger. For both cases, the variation of the dielectric constants were similar. The values calculated by SPW method were in general larger than the ellipsometric values for thinner (< 30 nm) and smaller for thicker films. The SPW results were in good agreement with the literature [20-21]. The lineshape of the SPW resonance is influenced by grating profile, by the substrate on which grating is defined as well as by the presence of very thin Al_2O_3 films on Al films, effects of all of these variations are evaluated in the following sections.

6a. INFLUENCE OF GRATING PROFILES

In our work, the depth of the grating was chosen to keep the coupling strength well within the Rayleigh criterion ($h/d = .07$). In Fig. 6, we have calculated SPW lineshapes for three different profiles assuming same period ($d=477$ nm), depth ($h=16$ nm), and dielectric constant ($\epsilon=46,16$), the difference in profile changes coupling efficiencies, but there are no significant changes in the resonance angles and widths. In addition to the grating profile, the substrate in which the grating is fabricated also plays an important part. In Fig. 7, we have shown experimental and calculated SPW lineshapes for 50-nm thick Al films deposited on Si ($h=16$ nm), SiO_2 ($h=17$ nm), and photoresist ($h=36$ nm) gratings. The profiles of these gratings are shown in Fig. 8. The dielectric constants of the films on SiO_2 and photoresist are characterized by (-40.1,14.6) and (-32.2, 12.8). It is seen that dielectric constant of the film deposited on photoresist is significantly different from the values in Table 1. This suggests that the photoresist surface being significantly rougher than either SiO_2 or Si results in the growth of poor quality films.

6b. INFLUENCE OF OXIDE LAYERS

When a freshly deposited Al-film is exposed to the atmosphere at room temperature, a transparent, amorphous oxide layer immediately forms on the metal surface. Hass reported that the oxide within a few hours grows to a thickness of approximately $15\text{-}20$ Å, but further growth occurs slowly reaching a maximum of 45 Å after one month [22]. In order to investigate the influence of Al oxide film on the SPW resonance lineshape of Al

films, we deposited very thin (5-20 Å) films of Al_2O_3 on an approximately 40-nm thick Al film. In Fig. 9, we have shown the results of 5 and 20 Å oxide on the SPW lineshape. The solid line represents bare Al film (thickness = 40 nm, Fig. 3c). 5 Å oxide film significantly alters the SPW resonance characteristics increasing the resonance width by 17%, resonance angle by 6%, and decreasing coupling efficiency by 11%. The corresponding numbers for 20 Å film were 31%, 25%, and 21%. Assuming the dielectric constants of bulk Al [21] in literature (46.36, 16.69), our calculations showed that the resonance angle was $.6^\circ$ in comparison with the corresponding values of $.74^\circ$ and $.76^\circ$ for evaporated and sputtered films (thickness = 50 nm). Assuming an oxide layer of 20 Å ($n = 1.66$) on bare Al substrate, our calculations showed that the resonance angle increased by $.16^\circ$, which is in good agreement with our data. However, deposition of 5-20 Å Al_2O_3 resulted in increases in resonance angles which were almost twice $.32^\circ$. Therefore, it appears that the oxide film is not limited to the surface, but also penetrates in the Al film and changes its composite dielectric constant. This is reflected in the much higher resistivity of oxide coated films as will be shown later.

7. SEM MEASUREMENTS

Grain boundaries, voids, and other inhomogeneities significantly affect the optical properties of thin films [23-24]. This is reflected in the large differences of the dielectric constants of the films (Table 1). In Fig. 10, we have shown a series of scanning electron micrographs (SEMs) of the Al films as a function of thickness. The increase in grain sizes is consistent with similar behavior for metal films, such as silver [25]. The grain sizes and boundaries for evaporated films (Fig. 10a) are significantly larger than the films deposited by sputtering and ion-assisted sputtering (Figs. 10b & 10c). For evaporated films, the film discontinuities decrease rapidly with thickness, and also the film surface appears very smooth. The behavior of both sputtered and IAS films is different; the grain size increase with film thickness is slow, and the film surface appears rough and discontinuous. These results indicate that the process of film growth by evaporation and sputtering is fundamentally different. In evaporated films, the grain boundaries are interconnected, the individual grains are not spherically symmetric, and the structure as a whole appears continuous. With sputtered and IAS films, however, the grain boundaries are not interconnected, the individual grains are approximately spherical, and the structure as a whole appears

discontinuous. The dielectric response (Table 1) of these films provides us with a simple means of calculating the density of the films [3]. Using the Bruggeman effective medium approximation [26], it is possible to define an effective dielectric constant, ϵ , for the film in terms of the bulk dielectric constant ($\epsilon_{\text{met}} = 46.36, 16.69$) and the volume fraction of voids in the film.

$$\epsilon = \frac{(2X-1) + \epsilon_{\text{met}}(2-X) + \sqrt{[(2X-1) + \epsilon_{\text{met}}(2-X)]^2 + 8\epsilon_{\text{met}}(1+X)^2}}{4(1+X)}, \quad 10.$$

where X is the ratio of void volume fraction to the metal volume fraction. Using this equation, and given the measured dielectric constants in table 1, we calculated the void fractions of 0.01, 0.06, and 0.17 for evaporated, sputtered, and IAS films. For thinner films (< 20 nm) corresponding measured dielectric constants (Table 1) were not in good agreement with calculated values from Eq. 10 for any value of X . A comparison of the structures of sputtered and IAS films (Figs. 10b & 10c) shows that the film morphology is very similar for both films, and therefore the large void fraction difference as predicted by Eq. 10 is misleading. This, coupled with increasing disagreement for thinner films, suggests that the Bruggeman effective media approximation is not appropriate to describe the composite metal structure. As will be seen in the next section, the structural changes at the grain boundaries play a major role in determining the dielectric properties.

8. RESISTIVITY MEASUREMENTS

Resistance measurements provide information about the internal structure of the metal films [24]. Using standard four-point probe technique [27], the resistivity of all films for which optical measurements had been performed was determined. In Fig. 11, the resistivity is plotted as a function of film thickness. The solid and dotted lines are the result of theoretical modeling and will be discussed below. From the data, the following salient features are apparent:

1. for evaporated films, the resistivity ratios, i.e., film resistivity/bulk resistivity, where $\rho_b = 2.73 \mu \Omega\text{-cm}$ [28] varied from 11.24 to 1.18 for film thickness increasing from approximately 7 to 100 nm;

2. for sputtered films, the resistivity ratios varied from 36 to 2.65 as film thickness increased from 5 to 50 nm, and;

3. for IAS films, the resistivity ratios varied from 13 to 3.96 as film thickness increased from 6 to 100 nm.

The resistivity of vacuum deposited thin metal films depends on the thickness, grain size, and the impurities present in the film. Various theories have been developed to account for the thickness variation of the resistivity [29-34]. In the Fuchs-Sondheimer (F-S) theory [29], assuming free electron model the increase in the resistivity of the film with decreasing film thickness is modeled by assuming that the electron scattering at the film surfaces modifies the electron distribution resulting in an expression for the thickness dependence of the resistivity. This theory, however, shows small thickness dependent contribution for films thicker than the mean free path of the electrons. For films much thinner than the electron mean free path, Lovel and Appleyard (L-A) also developed an expression for resistivity dependence of thickness [30]. We have not been able to fit our data with either of these theories. In F-S theory, the high resistivity ratios obtained experimentally force the calculations to pick abnormally high mean free paths reducing the applicability of the theory to either very low temperatures, or to very thick films at room temperatures. The L-A theory is not suitable for the range of film thicknesses in our experiment. We therefore used a very simple empirical expression due to Planck [35] to fit our resistivity data for the films. According to this expression, the film resistivity as a function of thickness is simply given by

$$\rho_t = \rho_b \left(1 + \frac{A}{t}\right)$$

11.

where ρ_t is the thickness dependent resistivity, ρ_b is the bulk resistivity, and t is the film thickness. The constant A was later specified to be $4 l_e / \pi$, where l_e is the electron mean free path, by simply averaging over the reduction of electron mean free path for film thickness less than the electron mean free path [36]. For films thicker than the mean free path, a smaller value of $A \sim 3 l_e / 8$ is appropriate since some of the electrons are not stopped by the film surfaces [31]. In Fig. 11a., we have plotted Eq.11 with $A = 4 l_e / \pi$ for mean free paths of 14 nm (dotted line), as calculated from basic principles [37, 28] and 30 nm (solid line) as given by Mayadas, et al.

[33]. With $l_e = 14$ nm, the fit is better for thicker films (40-60 nm), while for thinner films, the fit is better at $l_e = 30$ nm. The same calculation, however, does not predict the higher resistivities found for sputtered and IAS films (Table 1). Therefore, in addition to thickness dependence, there is also structure (grain size, boundaries, defects, etc.) dependence of resistivity. According to Mathiessen's rule [36], the total resistivity of the metal film can then be expressed as the sum $\rho = \rho_l + \rho_g$ where ρ_g is the resistivity due to the scattering of electron by lattice defects, grain size, and impurities, and ρ_l is given by Eq. 11. For films deposited by different techniques ρ_l shows approximately similar behavior. The grain-dependent resistivity, ρ_g , varies according to the growth conditions of the film. Mayadas and Shatzkes developed a model to predict qualitatively the effects of grain boundary scattering [33]. Their calculations showed that the measured resistivities increase significantly due to the scattering from the grain boundaries. In this model, the grain boundaries are represented as partially reflecting surfaces normal to the plane of the film, separated by an average distance D . The ratio between the grain and the bulk resistivity is given by

$$\frac{\rho_g}{\rho_b} = 1 - \frac{3\alpha}{2} + 3\alpha^2 - 3\alpha^3 \ln(1+\alpha^{-1}),$$

12.

where α is defined by $(\frac{l_e}{D} \frac{R}{1-R})$ with R being the electron reflection coefficient at the reflecting planes (corresponding to grain boundaries). From the SEM analysis, it is evident that the distance D , which has also been identified as grain size, is similar for both sputtered and IAS films. Therefore, the increased contribution to resistivity appears to come from increased reflectance at the grain boundaries. In Figures 11b & 11c, we have plotted the sum $\rho = \rho_l + \rho_g$ for $R = .05$ and $.65$. It is seen that a reasonably good agreement is obtained with 30 nm mean free path. The large value of R for IAS films suggests that the ion bombardment during sputtering results in significant changes in the shape of the Fermi surface, and the potential barrier at the grain boundaries. Similar behavior has been observed for Ag films by Parmigiani, et al. [7]. Finally, in Fig. 12, we have plotted the measured resistivities as a function of SPW resonance angle and width. The experimental data of Fig. 12a represents five films of approximately 40-nm thickness deposited by thermal evaporation, magnetron sputtering, Ion-assisted sputtering, and sputtered films with 5 and 20 Å Al_2O_3 films. The solid line presents a first order

polynomial fit thru the data points. The increase in resonance angle corresponds to a similar increase in film resistivity providing an excellent non-invasive monitor for film characterization. Similar behavior is also observed by plotting the SPW resonance width versus film resistivity as thickness is increased from 10-60 nm for thermally evaporated films (Fig. 12b). This shows that the wider the resonance, the larger is the film resistivity. Both of these parameters (Res. angle and width) are related to the film dielectric constants, which are related to the resistivity. For metals with imaginary part of the dielectric constant much smaller than the real part (Au, Ag, etc.) simple analytical relationships exist between resonance parameters and the dielectric constants. In case of Al, however, it is not possible to determine a simple analytical relationship. Our calculations and the experimental data (Figs. 12a & 12b), however, suggest a linear response of resistivity with increase in resonance angle and width.

9. CONCLUSIONS

A detailed investigation of the optical, structural, and electrical properties of Al films in the 5-60 nm thickness range has been carried out. The measurement of metal film optical properties using grating excitation of SPWs is shown to provide simple, readily interpretable results. The influence of different substrates and profiles has been investigated. A comparison of the film structure of evaporated, sputtered, and IAS films by SEM analysis, and optical measurements suggests that a description of effective medium dielectric constant in terms of the presence of voids is inappropriate. A comparison of the electrical resistivities shows that the scattering from the grain boundaries substantially increases the resistivities of the films grown by ion-bombardment. It has been shown by Zieman et al. [38] that for the films grown under ion-bombardment, two distinct regimes exist: one regime where resistivity increases and grain size decreases with increasing energy delivered to the substrate during deposition process, and the second regime, which occurs at higher deposition rates where the reverse behavior is observed. The experimental data presented here show that these films correspond to the the first regime where energy delivered to the substrate increases from evaporated to IAS films along with an increase in resistivity, although our SEM measurements did no show a significant change in the grain sizes of IAS films. It is suggested that the increased resistivity of the sputtered and IAS films is due to an increase in grain boundary reflectance.

APPENDIX

The boundary conditions at the two interfaces, metal-air and metal-substrate, are given by

$$B_{vac} - B_{met} = 0, \quad 1.$$

$$B_{met} - B_{sub} = 0, \quad 2.$$

$$\left(\frac{\partial}{\partial n} - \frac{1}{\epsilon_{met}} \frac{\partial}{\partial n} \right) (B_{vac} - B_{met}) = 0, \quad 3.$$

$$\left(\frac{\partial}{\partial n} - \frac{1}{\epsilon_{sub}} \frac{\partial}{\partial n} \right) (B_{met} - B_{sub}) = 0, \quad 4.$$

where

$$\frac{\partial}{\partial n} = \sqrt{1 + \left(\frac{\partial f(y)}{\partial n} \right)^2} \left(\frac{\partial}{\partial z} - \frac{\partial f(y)}{\partial y} \frac{\partial}{\partial y} \right). \quad 5.$$

On applying these boundary conditions at $z = -t + uf(y)$ and $z = uf(y)$, where u is the grating amplitude and $f(y)$ defines the grating profile, and taking the Fourier transform of the resulting set of equations, one arrives at the set of equations (5-8) given in the text. The Fourier transform integral (Eq. 9) for the grating profile (Fig. 5) can be solved analytically by assuming that in the region $\pm b_1 d/2$ to $\pm b_2 d/2$, the grating profile can be described by the straight line equation $y = mx + c$, with $m = \frac{\pm 4u/d}{b_1 - b_2}$, and $c = \frac{b_1 + b_2}{b_1 - b_2}$, where b_1 and b_2 were determined from SEM measurements (Fig. 7c) to .606 and .367 respectively. The integral in Eq. 9 can therefore be evaluated for $p=0$ as

$$X_0(p) = \exp(-p) (1 - b_1) + \exp(p) b_2 + \frac{r_1 \exp(pr_2)}{2p} (\exp(-2pr_1) - \exp(-2pr_2)). \quad 6.$$

and for $p \neq 0$,

$$\begin{aligned}
 X_p(\rho) = & \frac{i \exp(-\rho)}{2\pi p} (\exp(i\pi p b_1) - \exp(-i\pi p b_1)) + \frac{i \exp(\rho)}{2\pi p} (\exp(-i\pi p b_2) - \exp(i\pi p b_2)) \\
 & + \frac{\exp(pr_2)}{\frac{4p}{r_1} + i 2\pi p} (\exp[-(\frac{2p}{r_1} - i\pi p)b_2] - \exp[-(\frac{2p}{r_1} + i\pi p)b_2]) \\
 & + \frac{\exp(pr_2)}{\frac{4p}{r_1} + i 2\pi p} (\exp[-(\frac{2p}{r_1} + i\pi p)b_2] - \exp[-(\frac{2p}{r_1} + i\pi p)b_1]). \tag{7}
 \end{aligned}$$

with $r_1 = \frac{b_1 - b_2}{r_2}$, $r_2 = \frac{b_1 + b_2}{r_1}$, $r_3 = \frac{b_2}{r_1}$, $r_4 = \frac{b_1}{r_1}$, and ρ is defined in the text. For a square profile, Eqs. 6 and 7

assume much simpler forms.

$$X_0(\rho) = \cosh(\rho), \tag{8}$$

and

$$X_p(\rho) = \frac{2i}{\pi p} \sinh(\rho) \sin\left(\frac{\pi p}{2}\right). \tag{9}$$

ACKNOWLEDGEMENTS

This work was supported by SEMATECH / SRC. We would also like to acknowledge the assistance of Alfonso Torres, Chris Krannenberg, Scott Wilson, Susan Hietala, M. Yousaf, and Mike Lang during the course of this work.

1. B. Draper is with the Sandia National Laboratories, Albuquerque, New Mexico.
2. J. R. McNeil is with the Department of Electrical Engineering, University of New Mexico.
3. S. R. J. Brueck is with the Departments of Electrical Engineering and Physics, University of New Mexico.

REFERENCES

- Archer, J. O. S. A. 52, 970 (1962).
- Aspness and A. A. Studna, Phys. Rev. B 27, 985 (1983).
- Aspness, Thin Solid Films 89, 249 (1982).
- Johnson and R. W. Christy, Phys. Rev. B 6, 4370 (1973).
- King and S. P. Talmi, Optica Acta 28, 407 (1981).
- Zhizhin, M. A. Moskalova, E. V. Shomina, and V. A. Yakovlev, 1980a, Fiz Met i Met 50, N3.
- Parmigiani, E. Kay, T. C. Huang, J. Perrin, M. Jurich, and J. D. Swalen, Phys. Rev. B 33, 879 (1986).
- Fuzi, G. W. Bradberry, and J. R. Sambles, Jour. Mod. Opt. 36, 1405 (1989).
- Kretschmann and M. Raether, Z. Naturf (a) 24, 2135 (1968).
- Otto, Z. Phys. 261, 398 (1968).
- Electromagnetic Surface Modes, Edited by A. D. Boardman, Wiley (1982).
- Surface Polaritons, Edited by V. M. Agranovich and D. L. Mills, North-Holland (1982).
- Saleem H. Zaidi, M. Yousaf, and S. R. J. Brueck, J. O. S. A. B 8, 770 (1991).
- Saleem H. Zaidi, M. Yousaf, and S. R. J. Brueck, J. O. S. A. B 8, 1348 (1991).
- Mcnally, J. R. McNeil, J. M. Bennett, and H.H. Hurt Appl. Opt. 25, 3631 (1986).
- Saleem H. Zaidi and S. R. J. Brueck, Appl. Opt. 27, 2999 (1988).
- Urban III, Applied Surf. Sci. 33/34, 934 (1988).
- Toigo, A. Marvin, V. Celli, and N.R. Hill, Phys. Rev. B 15, 5618 (1977).
- Hill and V. Celli, Phys. Rev. B 17, 2478 (1978).
- Schulz, J. O. S. A. 44, 357 (1954).
- Optical Properties of Metals, G.P. Motulevich, Consultants Bureau (1973).
- Hass G., Z. Anorg. Chem. 254, 96 (1947).
- Optical Properties of Thin Solid Films, O. S. Heavens, Dover Publications Inc. (1955).
- Vacuum Deposition of Thin Films, L. Holland, Wiley (1969).
- Sennet and G. D. Scott, J. O. S. A. 40, 203 (1950).

- G. Bruggeman, Ann. Phys. (Leipzig) 24, 636 (1935).**
- Smits, Bell Sys. Tech. Journal, 711 (1958).**
- Handbook of Physics and Chemistry, edited by West, CRC Press (1989-90).**
- Sondheimer, Advan. Phys. 1, 1 (1952).**
- S. Appleyard and A. C. B. Lovell, Proc. Roy. Soc. A 158, 718 (1937).**
- Chopra and L. C. Bobb, Acta Metallurgica 12, 807 (1964).**
- Mayadas, Jour. Appl. Phys. 39, 4241 (1968).**
- Mayadas and M. Shatzkes, Phys. Rev. B 1, 1382 (1970).**
- Mayadas, M. Shatzkes, and J. F. Janak, Appl. Phys. Lett. 14, 345 (1969).**
- Wilkinson, Jour. Appl. Phys. 22, 419 (1951).**
- Weale, Proc. Roy. Soc. Lon. A 62, 135 (1949).**
- Solid State Physics, N. W. Ashcroft, Holt, Rinehart and Winston (1976).**
- Ziemann and E. Kay, J. Vac. Sci. Tech. A 1, 512 (1983).**

TABLE 1 Dielectric constants and dc resistivities of Al as a function of film thickness for evaporated, sputtered, and IAS films.

**TABLE 1. OPTICAL PARAMETERS AND dc RESISTIVITIES
AS A FUNCTION OF FILM THICKNESS**

Film Thickness (nm)	Ellip. Measurements (ϵ_r, ϵ_i)	SPW Measurements (ϵ_r, ϵ_i)	Resistivity (10 ⁻⁶ Ω -cm)
1. Evaporated Films			
7.5	(-33.1, 15.3)	-----	30.7
10.	(-28.8, 17.9)	(-36, 20)	18.
18.	(-42.1, 16.1)	(-42.6, 14.9)	7.9
29.	(-44.8, 16.3)	(-40.1, 14.2)	5.6
40.	(-45.1, 16.5)	(-40. 14.8)	4.2
52.	(-44.3, 16.6)	(-41.4,15)	4.1
2. Sputtered Films			
5.2	(-13.7, 13.4)	-----	98.8
11.	(-29.2, 15.2)	(-33., 22.)	18.8
15.	(-36.4, 15.4)	(-39.5, 16.5)	15.3
20.	(-34.8, 14.)	(-36.5, 14.)	16.1
30.	(-40.6, 14.2)	(-37.7,14.8)	8.9
40.	(-41.1, 15.4)	(-40.1,14.6)	7.5
50.	(-40.8, 15.)	(-40.3,14.7)	7.2
3. IAS Films			
6.1	(-27.7, 17.4)	-----	36.5
13.5	(-28.2, 15.7)	(-32.2, 15.8)	30.4
21.	(-30.2, 11.8)	(-33., 13.8)	21.4
31.	(-28.3, 12.2)	(-30., 13.5)	20.7
42.	(-33.3, 12.8)	(-33,13)	14.6
55.	(-29.2,11.4)	(34.1, 12.8)	17.4
73.	(-32.8,12.7)	(-31.3, 12.5)	9.6

FIGURE CAPTIONS

Fig. 1. Experimental variation of ellipsometric parameters Δ and Ψ with film thickness for Al films deposited by three different techniques.

Fig. 2 Variation of SPW lineshape for Al film thickness from 5 to 20 nm.

Fig. 3 Variation of SPW lineshape for Al film thickness from 24 to 50 nm.

Fig. 4 Experimental variation of SPW parameters, coup. eff., res. width, and res. angle shift, with film thickness for films deposited by three different techniques.

Fig. 5 Profile of the Si grating used for numerical calculations.

Fig. 6 Variation of the SPW lineshape for sinusoidal, square, and Fig. 5. grating profiles

Fig. 7 Variation of SPW lineshape for sputtered Al film (thickness = 50 nm) deposited on three different substrates.

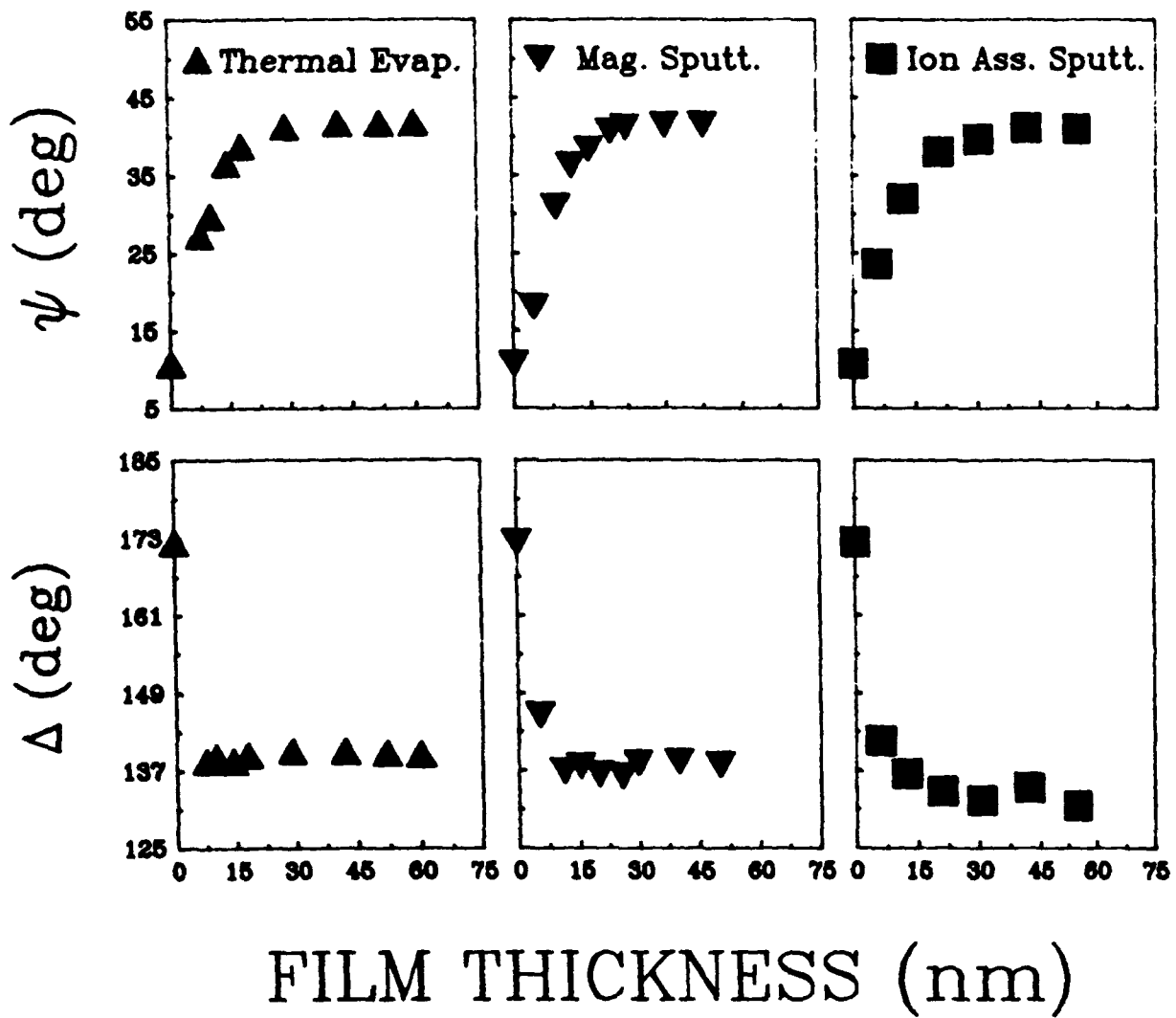
Fig. 8 SEM profiles of three gratings (Si, Photoresist, and SiO_2) used for SPW characterization.

Fig. 9 Influence of thin oxide films on SPW lineshape of approximately 40 nm sputtered Al films.

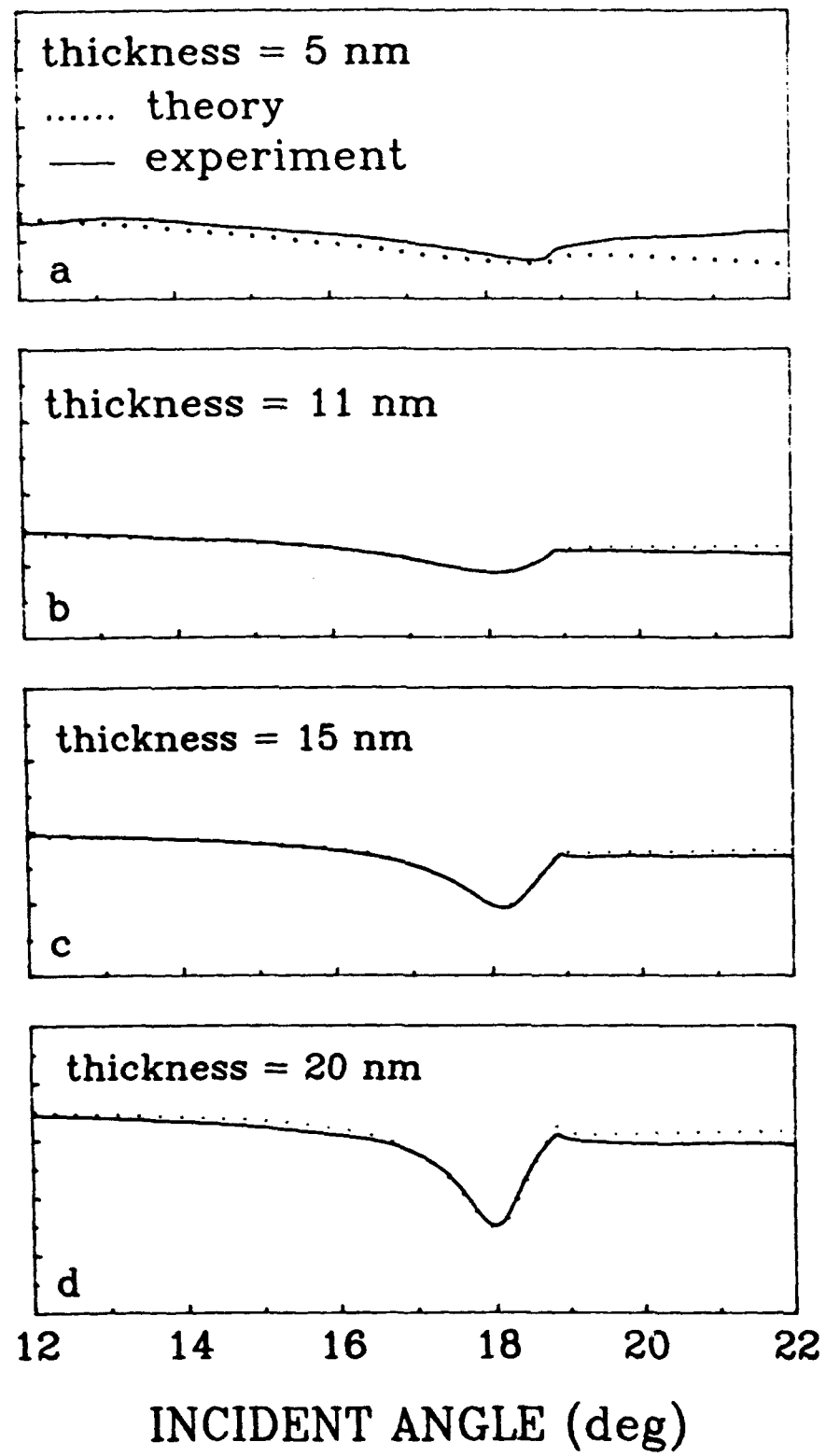
Fig. 10 SEM measurements of Al films deposited by three techniques, a. thermal evaporation, b. magnetic sputtering, and c. ion-assisted magnetic sputtering.

Fig. 11 Variation of Al film resistivity with thickness and grain boundary reflection for films deposited by three different techniques assuming two different values of electron mean free path.

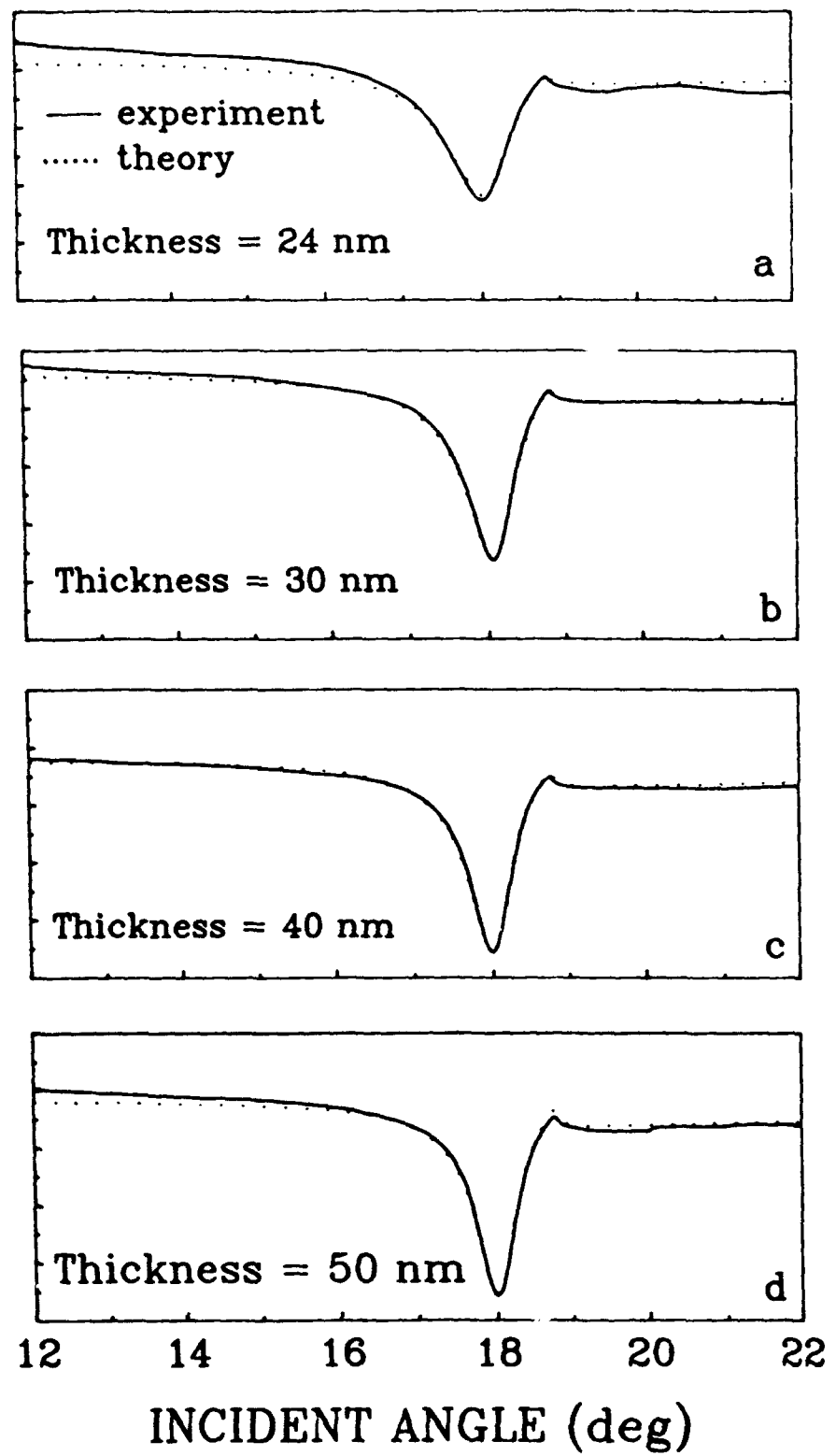
Fig. 12 Variation of Al film resistivity with SPW resonance angle for constant film thickness (a), and (b) resistivity variation with SPW resonance width for film thickness from 10 to 60 nm.

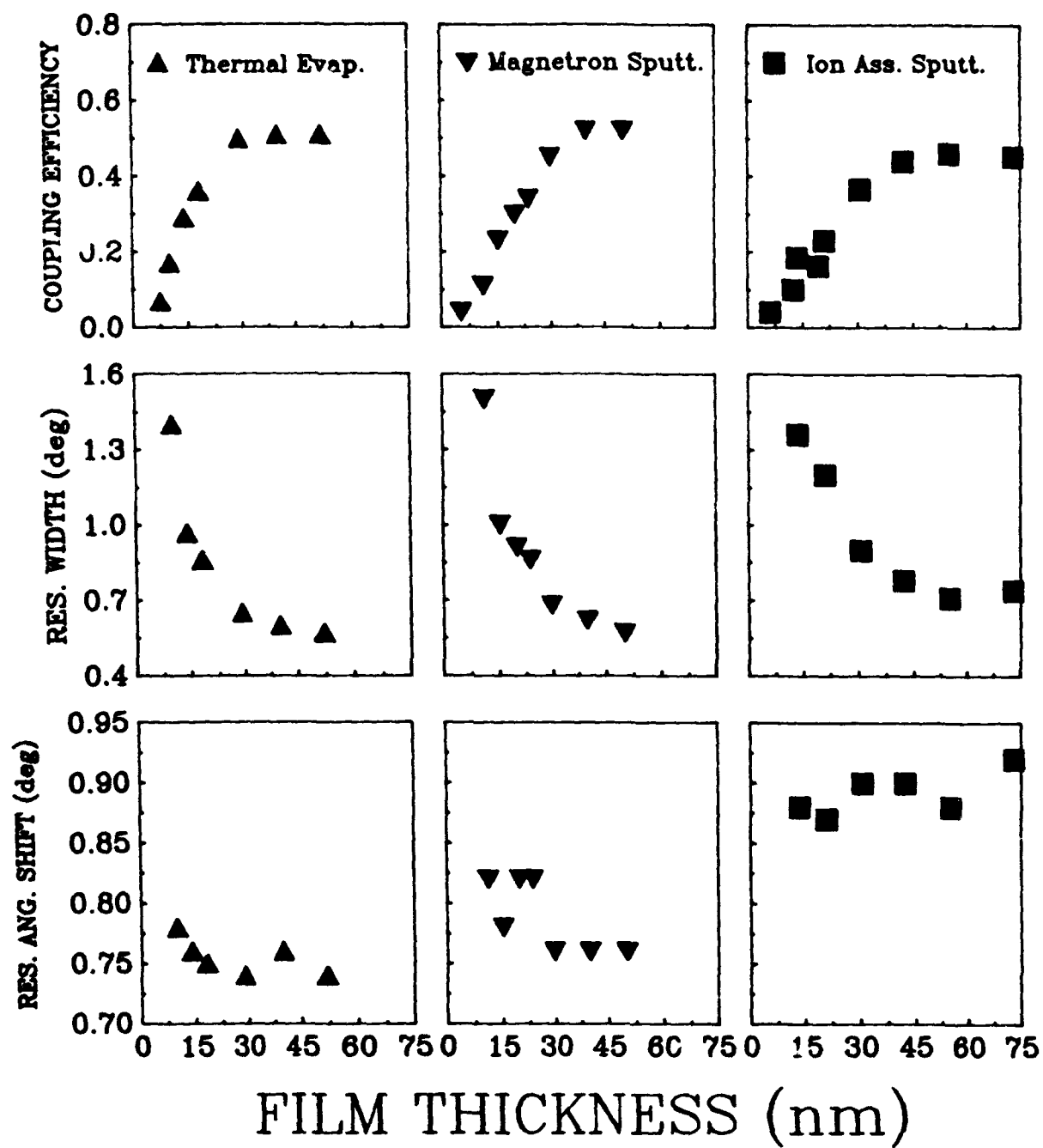


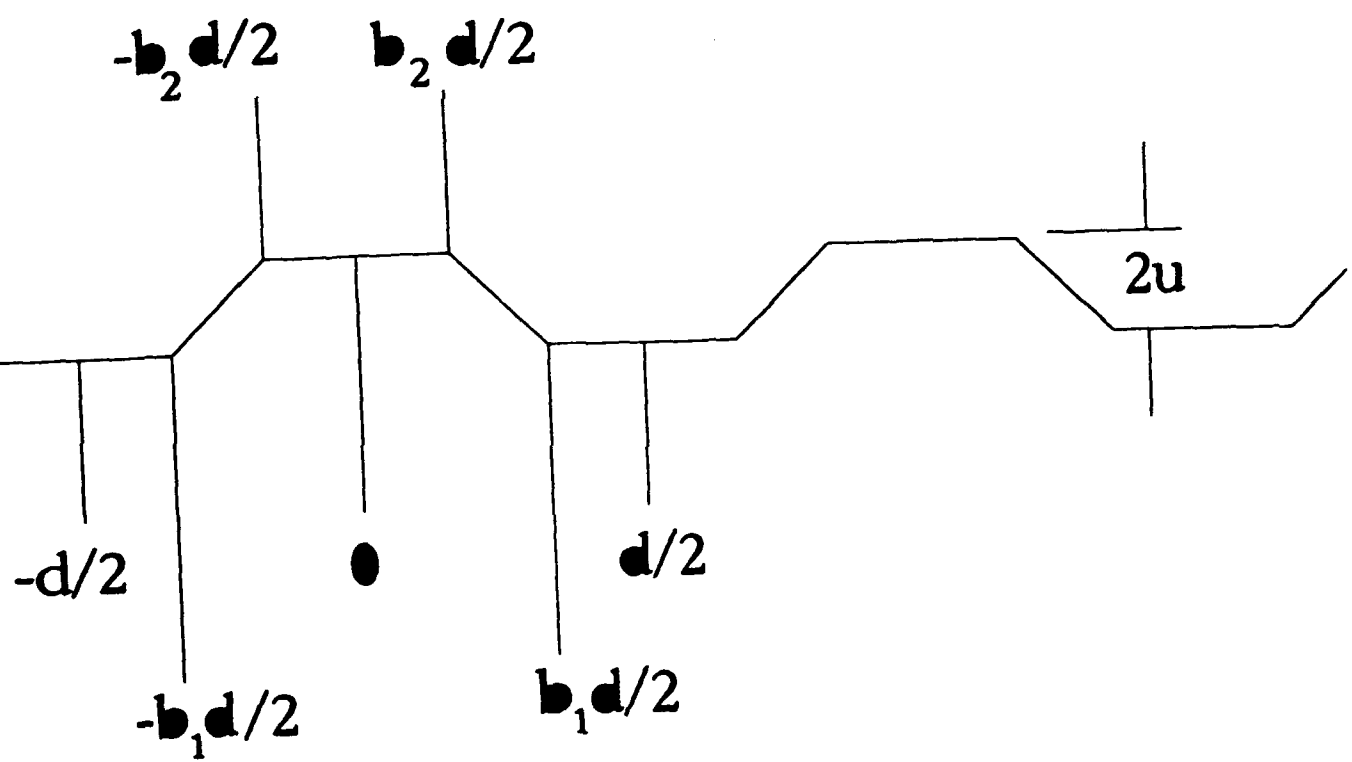
REFLECTANCE (a.u.)

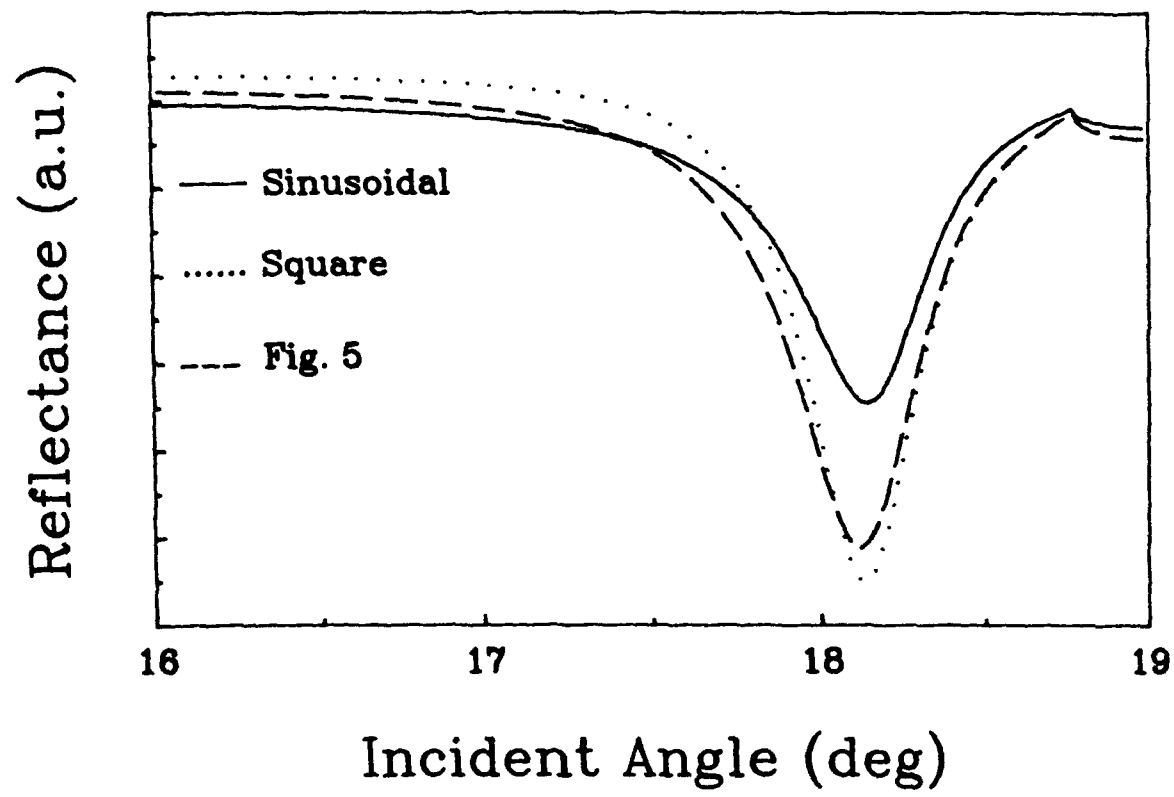


REFLECTANCE (a.u.)

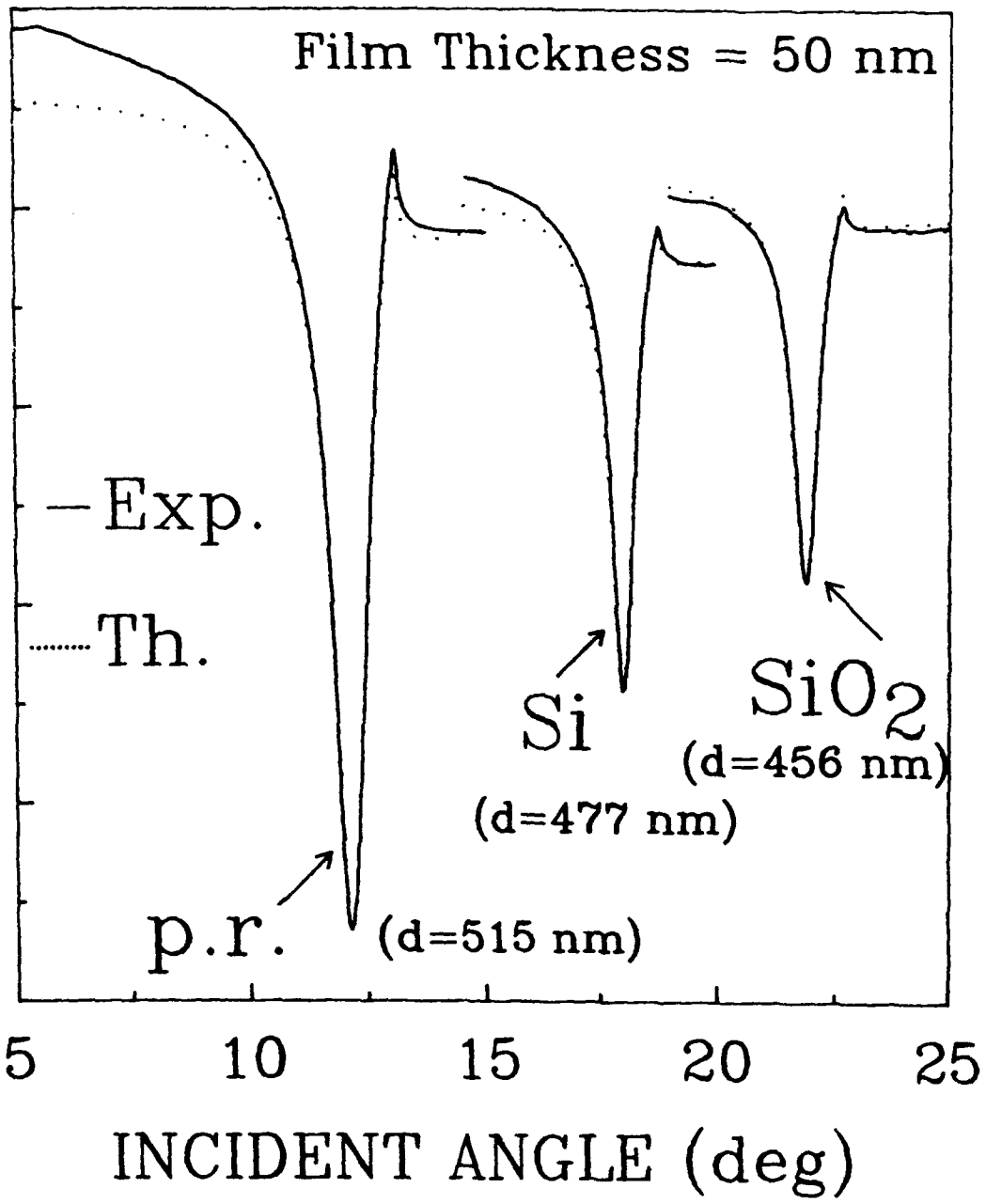




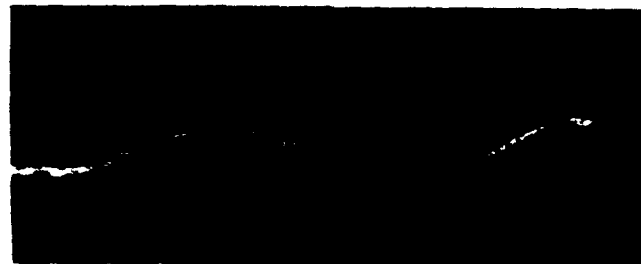




REFLECTANCE (a.u.)



SEM Profiles of gratings used for SPW characterization



Photoresist



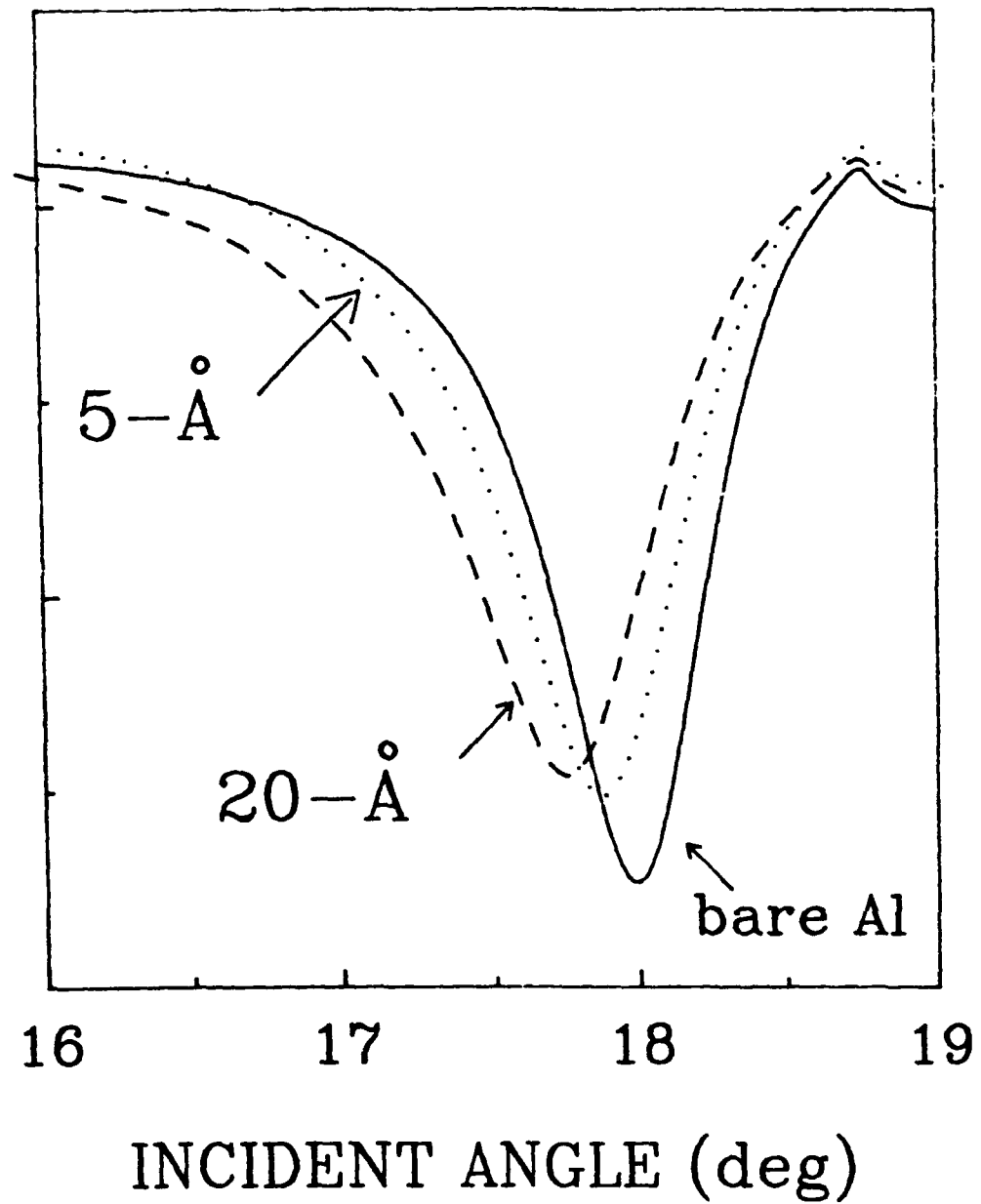
Si



SiO₂

000006 32kV 1100E 10.0μm

REFLECTANCE (a.u.)



Evap. Films

Thickness:

7nm



14nm



29nm



42nm



60nm



000046 25KV X1000 0.30µm

Sput. Films

Thickness:

5nm



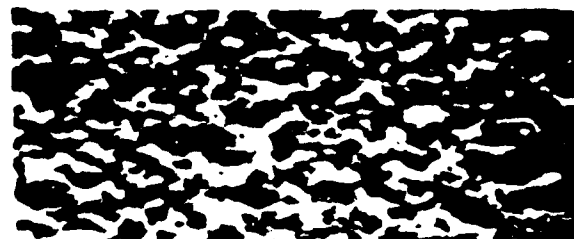
11nm



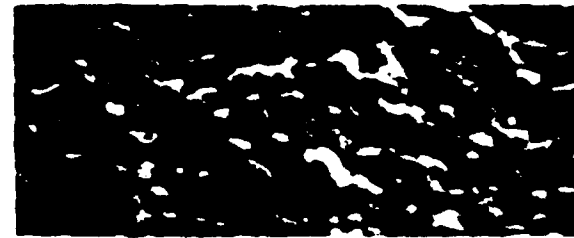
20nm



30nm



50nm



000025 25KV X100K 0.30um

IAS Films

Thickness:

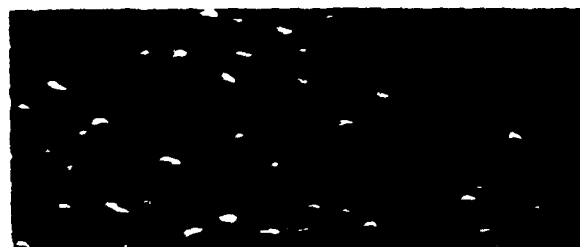
6nm



12nm



21nm



31nm



55nm



000001 25KV 11/06/01 00:00:00

